Proceedings of the
Annual Stability Conference
Structural Stability Research Council
Louisville, Kentucky, April 1-4, 2025

Flexural tests on high strength cold-formed steel solar piles

Fidence Cyizere Rukundo[1], Sophrenia David[2], Shahabeddin Torabian[3], Benjamin W. Schafer[4]

Abstract

This paper provides a summary of experimental work investigating the flexural strength of a highly optimized, locally stiffened, lipped channel section cold formed from high-strength low alloy steel. The primary use for the studied sections is for ground-based support of solar panel arrays, where flexural strength is a fundamental requirement. A series of four-point bending tests for both major-axis and minor-axis flexure are conducted. The section is unsymmetric about the minor axis so both positive and negative bending are required in this case. The sections are highly optimized against local and distortional buckling through the introduction of intermediate longitudinal stiffeners and return lips on the edge stiffeners. As a result, special care is required in the testing to develop local or distortional driven failure modes and restrict lateral-torsional buckling. In addition to the tests, stability of the section under major- and minor-axis bending is assessed using both shell finite elements and the finite strip method. Strength predictions for the section are assessed using the Direct Strength Method as implemented in the AISI S100 Specification and in papers proposing improved predictions for unsymmetric bending, and for handling buckling mode interactions that are more prominent in optimized high-strength steel specimens.

1. Introduction

In modern civil construction, cold-formed steel structures are widely utilized as both primary and secondary load-bearing members due to their high strength-to-weight ratio, ease of fabrication, and cost-effectiveness. However, these advantages come at the expense of increased susceptibility to instabilities, which are further amplified by initial geometric imperfections. To improve structural efficiency while maintaining economic and sustainability goals, there is a growing interest in replacing thicker, lower-strength steel with thinner, high-strength materials with complex cross-sectional geometries. However, the applicability of the Direct Strength Method (DSM)—a widely used approach for predicting the nominal capacity of cold-formed steel—to these optimized sections may require further study. This study examines the flexural behavior of channel sections with multiple stiffeners (Figure 1), cold-formed from high-strength low-alloy steel with a yield strength of 100 ksi (690 MPa). Previous research (Akchurin et al., 2023; Akchurin et al., 2025) has focused on the axial compressive strength and initial geometric

[1] Graduate Research Assistant, Johns Hopkins University, <fcyizer1@jh.edu>
[2] Graduate Research Assistant, Johns Hopkins University, <sdavid29@jh.edu>
[3] Associate Research Scientist, Johns Hopkins University, <torabian@jhu.edu>
[4] Professor, Johns Hopkins University, <schafer@jhu.edu>

imperfections of these sections. Building upon this work, the present study evaluates their minor- and major-axis flexural strengths, which are the primary requirements of these sections when utilized in support of ground-mounted solar arrays.

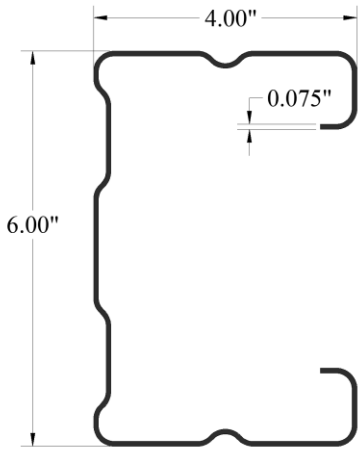

Figure 1. Nominal section(see Akchurin et al. (2023, 2025) for all dimensions)

To establish flexural capacities a series of four-point bending tests are conducted. As illustrated in Figure 1, the section is symmetric about the major axis, but unsymmetric about the minor axis. Minor-axis bending tests are divided into two sets: one in which the section lips are in compression (LIC) and another where the lips are in tension (LIT). Major-axis bending tests are performed under two configurations: one with decks fastened to the shear spans to restrain twisting and another without decks, allowing for unrestricted twisting. Beyond experimental testing, the stability of the sections under major- and minor-axis bending is analyzed using both the finite strip method (CUFSM) and the finite element method (Abaqus). Additionally, the experimental results are compared to flexural strength predictions obtained from the Direct Strength Method outlined in AISI S100-16 and the modified Direct Strength Method for unsymmetric sections proposed by Glauz & Schafer (2022).

2. Experimental setup

2.1 Minor Axis Bending Test Setup

A series of four-point bending tests were conducted to evaluate the flexural capacity of the section about its minor axis. Two specimen configurations were investigated: minor-axis flexure where the section lips (Figure 1) are in tension, and minor-axis flexure where the lips are in compression. The overall test schematic and the realized test configuration are shown for the testing with the lips in compression in Figures 2 and 3 and testing with the lips in tension in Figures 4 and 5. Unique care was taken to insure that the loading and supports did not lead to section deformations or web crippling, this was accomplished by running the section through short HSS sections (7 in. x 7 in. x ½ in. in section and 8 in. long) at the supports and load points. The HSS sections are bolted to the web of the test specimen, thus all local bearing is taken by the HSS and the shear and moment in the specimen may be developed without distortions.

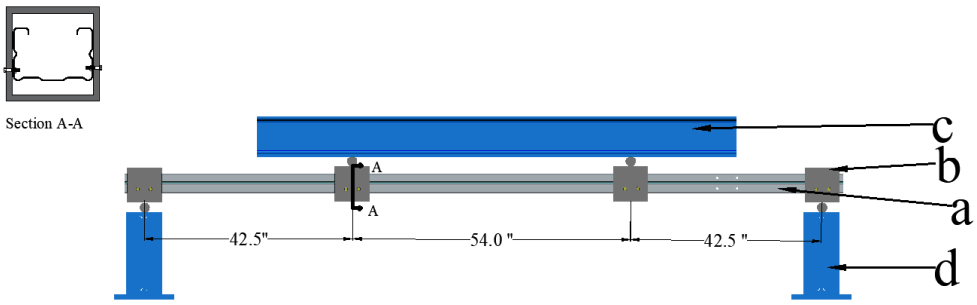

Figure 2. Elevation view of minor axis (LIC) test setup schematic: a. specimen, b. 7 × 7 × 1/2 HSS sections, c. spreader beam, d. end support beam

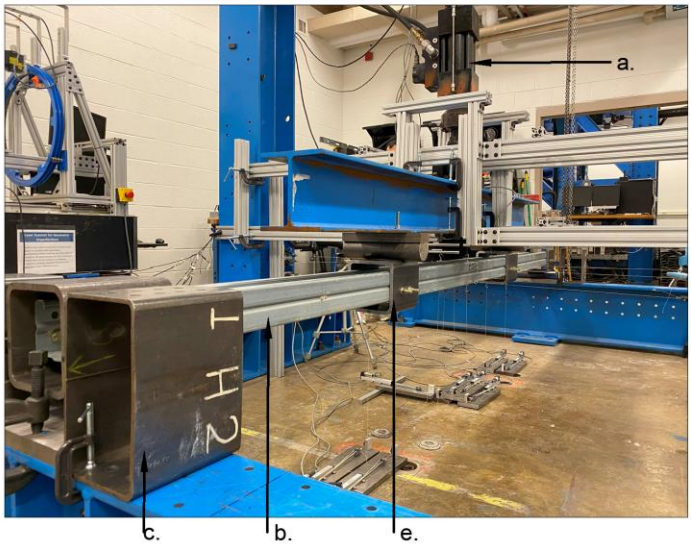

Figure 3. Minor axis bending test setup with lips in compression (LIC): a. actuator, b. specimen, c. lateral end supports, d. spreader beam, e. 7 × 7 × 1/2 HSS sections

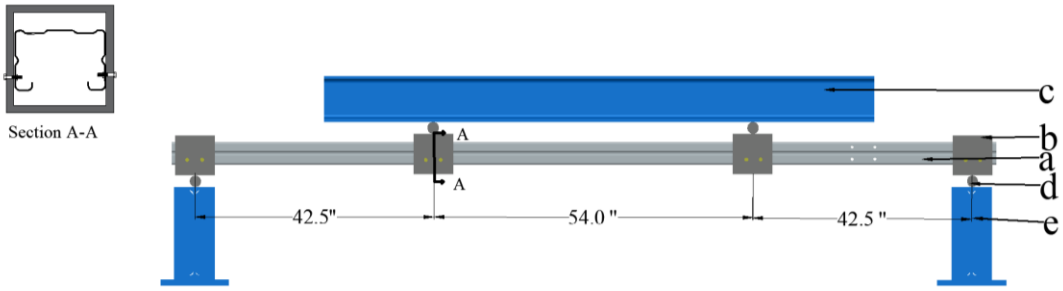

Figure 4. Elevation view of minor axis (LIT) test setup schematic: a. specimen, b. 7 × 7 × 1/2 HSS sections, c. spreader beam, d. rollers, e. end support beam

Figure 5. Minor axis bending test setup with lips in tension (LIT): a. actuator, b. aluminum frame, c. specimen, d. spreader beam, e. lateral PTs, f. ground PTs

2.2 Major Axis Test Setup

Figure 6 shows the test schematic of the major axis bending test and Figure 7 provides the realized test setup in the lab. To ensure a symmetric configuration and eliminate eccentric loading, each test utilized two opposing specimens. As shown, HSS sections were again used to avoid localized deformations at load application points and supports. Two sets of major axis bending tests were performed: (a) those conducted without steel deck panels fastened to the specimens (Figure 7), and (b) those conducted with steel deck panels fastened at the top and bottom of the specimens in the shear spans. The restraining effect of steel deck panels has been studied in previous research (Yu & Schafer, 2005, 2006, 2007). Here, the panels are used to eliminate twisting in the shear spans, as the goal of the testing is to determine the flexural capacity under pure moment.

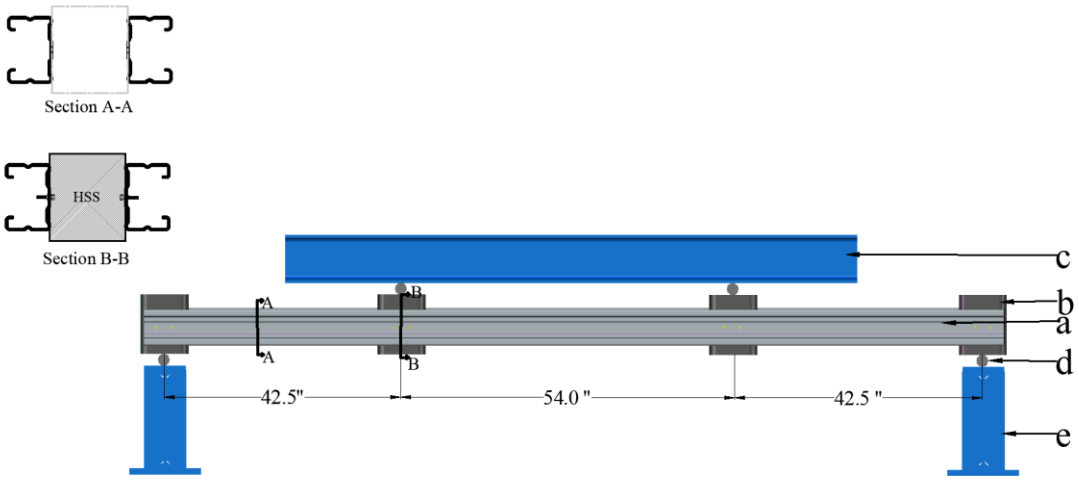

Figure 6. Elevation view of major axis bending test schematic: a. specimens, b. 7 × 7 × 1/2 HSS sections, c. spreader beam, d. rollers, e. end beam support

Figure 7. Annotated picture of major axis bending test setup with no steel panels: a. actuator, b. spreader beam, c. aluminum frame, d. specimen, e. lateral supports, f. end beam support, h. cameras

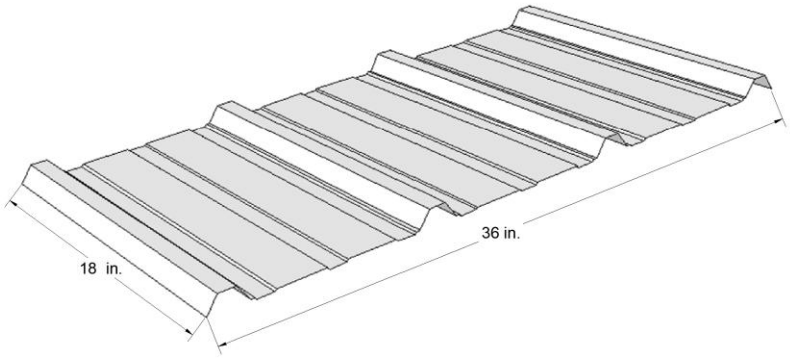

Figure 8. Standard steel deck panel

Figure 9. Major axis bending test setup with steel decks in the shear spans: a. specimen, b. steel panels, c. 7 × 7 × 1/2 HSS sections, d. lateral supports, e. end beam support

3. Elastic Buckling Analysis

To analyze the buckling behavior of the nominal section under bending, an elastic buckling analysis was conducted using the open-source software CUFSM (Adany, 2006; Li and Schafer, 2010). The study examined member instabilities under flexural loading for both major and minor axes. Signature curves illustrating local (L), distortional (D1, D2), and global (G) buckling modes are presented in Figures 11 through 13, with a summary of the buckling analysis results provided in Table 1.

Figure 10 shows the signature curve for minor-axis bending with the lips in compression. Two distinct distortional buckling modes (D1, D2), involving stiffeners, are highlighted. Figure 11 displays the signature curve for minor-axis bending with the lips in tension, showing separate local and distortional buckling modes. The global buckling modes, unorthodox to consider for minor-axis bending, but clearly shown in the signature curve response, involve cross-sectional distortions that do not strictly conform to the classical definition of global modes (Schafer & Adany, 2005). Nonetheless as they decrease to zero with length, these are still labeled as global modes (G).

Figure 12 presents the signature curve for major-axis bending. The curve shows a local buckling mode (L), two distinct distortional buckling modes (D1, D2) and the lateral-torsional buckling mode (G). Predicted global lateral-torsional buckling shapes from the shell finite element models that include the shear span, for both configurations, are shown in Figures 14 and 15. In CUFSM only the moment span is modeled; however, the boundary conditions at the end of the moment span (i.e., the loading points) for the major axis bending tests cannot be accurately modeled as either simple-simple nor fixed-fixed. When the shear spans are free (no deck) significant twist within the shear spans are observed in the elastic regime greatly influencing the behavior in the moment span. Supplemental shell finite element Abaqus models of the full test specimen length

(CUFSM models only considered the moment span) were utilized to study the global buckling behavior due to this twist for both sets of the major-axis bending tests.

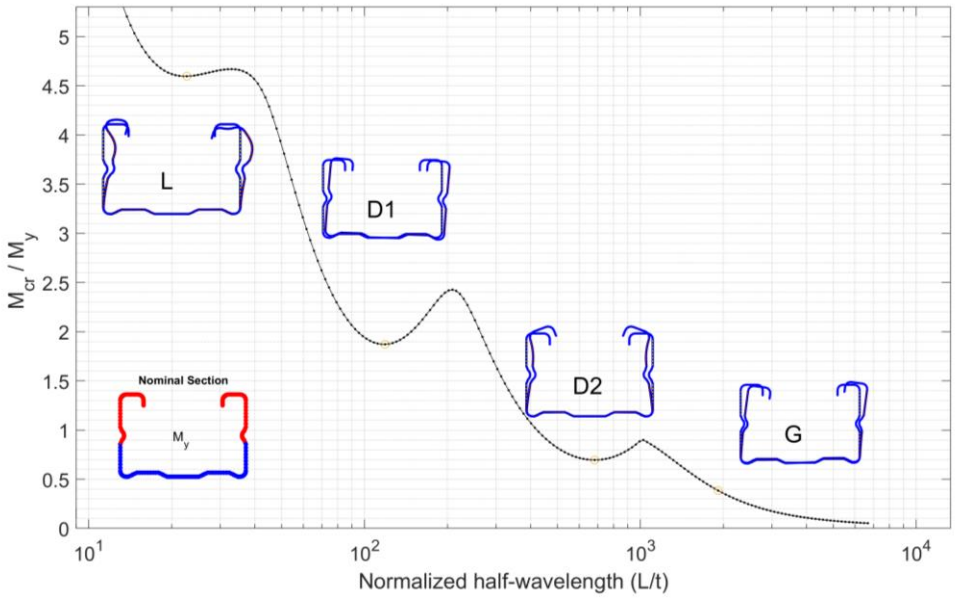

Figure 10. The signature curve of the nominal section under minor-axis bending with lips in compression: L, D, and G represent local, distortional, and global buckling modes. Fy = 101.4 ksi

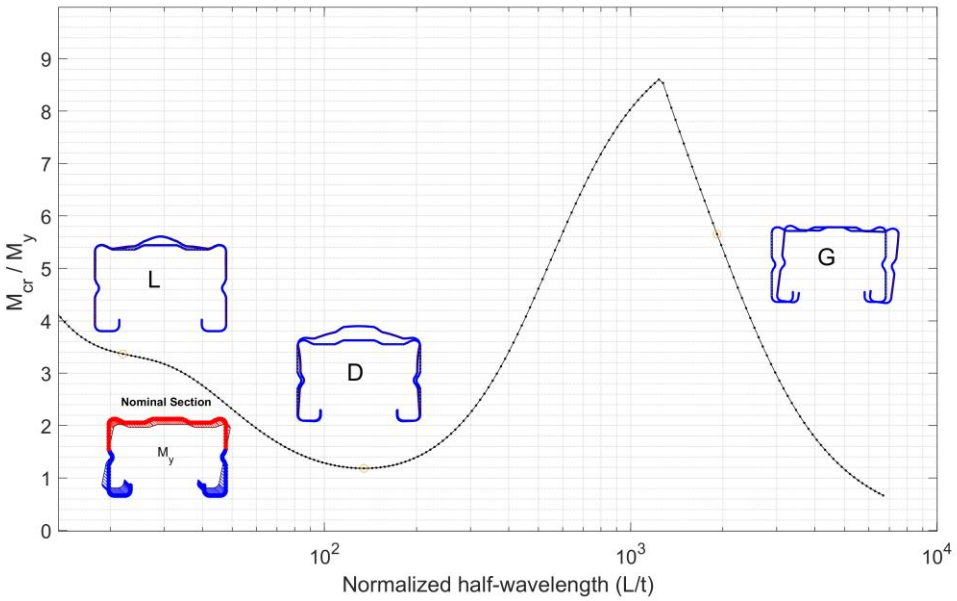

Figure 11. The signature curve of the nominal section under minor-axis bending with lips in tension: L, D, and G represent local, distortional, and global buckling modes. Fy = 101.4 ksi

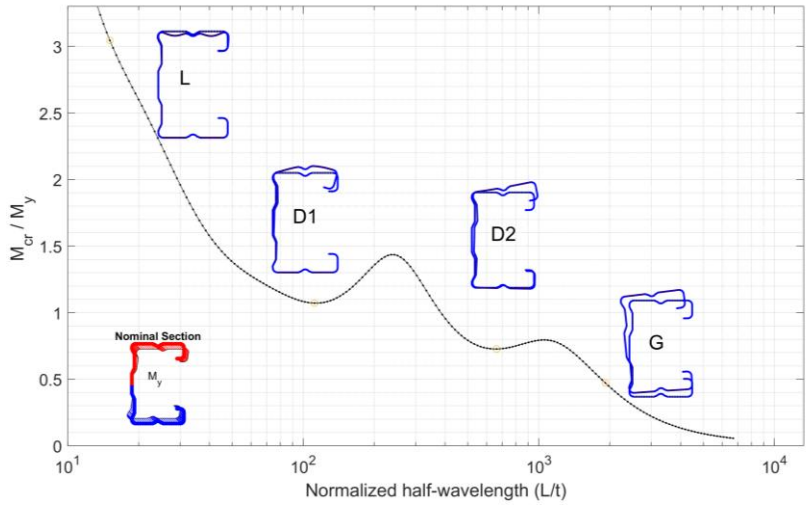

Figure 12. The signature curve of the nominal section under major axis bending action: L, D, and G represent local, distortional, and global buckling modes. Fy = 101.4 ksi

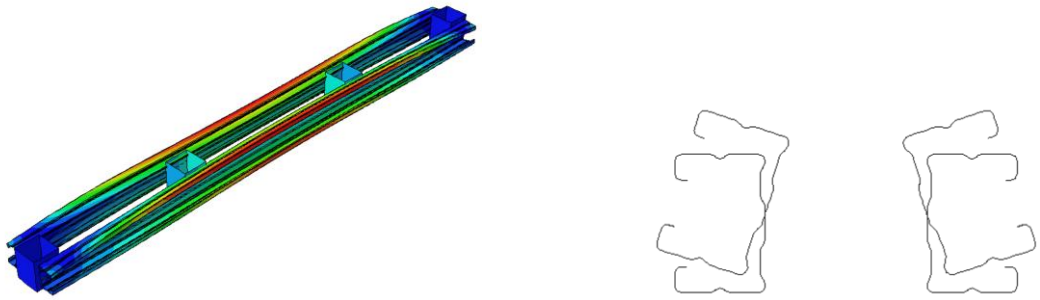

(a) (b)

Figure 13. Lateral torsional buckling mode of the members under major bending action from Abaqus (a) isometric view (b) midspan cross section (M_{cre}/M_y = 1.12)

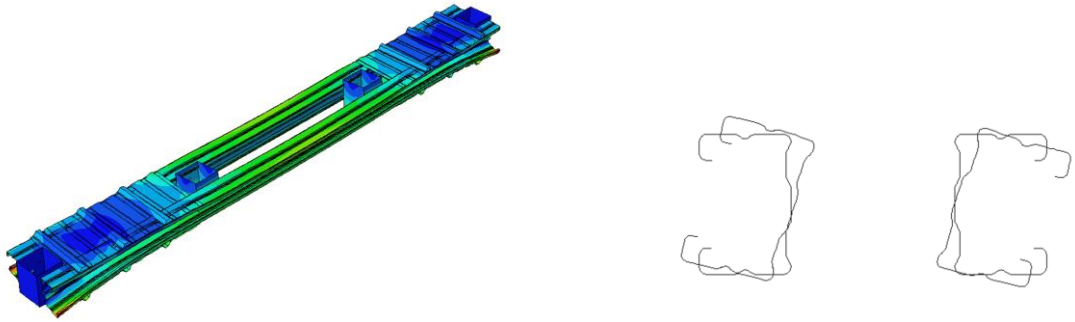

(a) (b)

Figure 14. Lateral torsional buckling mode of the members under major bending action with decks from Abaqus (a) isometric view (b) midspan cross section (M_{cre} /M_y = 2.35)

Table 1. Summary of buckling analysis

	L_{cr} (in.)				M_{cr}/M_y			
	L	**D1**	**D2**	**G**	**L**	**D1**	**D2**	**G**
Minor-axis (LIC)	1.70	8.91	51.2	54.0	4.60	1.87	0.70	2.89
Minor-axis (LIT)	1.65	10.10	-	54.0	3.37	1.18	-	49.51
Major-axis (w/o deck)	1.13	8.37	49.7	54.0	3.05	1.07	0.73	3.79[a] 1.12[b]
Major-axis (w/ deck)	1.13	8.37	49.7	54.0	3.05	1.07	0.73	3.79[a] 2.35[b]

a. CUFSM at L=54 in. with simply supported end conditions
b. ABAQUS shell FE of whole test specimen, with or without deck in shear span

4. Capacity Prediction Using Direct Strength Method

Table 2 summarizes the nominal strength calculation results using Direct Strength method. The nominal flexural strength of the section was predicted by the Direct Strength Method as implemented in the North American Specification for Cold-Formed Steel Structural Members (AISI S100-16). However, the section studied in this project is unsymmetric about the minor axis and the specification does not provide any adjustments for members which are unsymmetric about the axis of bending. Glauz and Schafer (2022) proposed modifications to the DSM method described in AISI S100, which were required due to stress redistribution associated with material and geometric nonlinearities. This report uses the DSM described in AISI S100-16, and the Glauz-Schafer (2022) modified DSM method, and the results are compared. It is worth noting that the major-axis nominal flexural strength for global buckling (M_{ne}) is calculated using the critical moment (M_{cre}) from Abaqus models; however, this local-global strength never controls.

Table 2: Direct Strength Method calculation results

	Parameters	**Minor axis (LIC)**	**Minor axis (LIT)**	**Major axis with no decks**	**Major axis with decks**
AISI S100-16 DSM	M_{nL} (kip-in)	124.3	124.3	212.4	249.4
	M_{nD1} (kip-in)	118.8	103.1	203.4	203.4
	M_{nD2} (kip-in)	84.9	-	176.6	176.6
	M_{ne} (kip-in)	125.4	124.3	212.4	249.4
	M_n (kip-in)	**84.9**	**103.1**	**176.6**	**176.6**
Glauz & Schafer (2022)	M_{nL} (kip-in)	153.4	156.2	216.2	254.6
	M_{nD1} (kip-in)	124.0	129.2	198.1	198.1
	M_{nD2} (kip-in)	93.2	-	174.6	174.6
	M_{ne} (kip-in)	125.4	173.5	212.4	249.6
	M_n (kip-in)	**93.2**	**129.2**	**174.6**	**174.6**

Note: M_{nL}: Nominal flexural strength for local buckling, M_{nD}: Nominal flexural strength for distortional buckling, M_{ne}: Nominal flexural strength for lateral-torsional buckling. For minor-axis bending: $M_{ne}=M_y$ for AISI S100-16 and $M_p= M_{ne}$ for Glauz & Schafer

5. Test Results

5.1 Test results of minor axis bending with lips in compression (LIC)

Figure 15 shows images illustrating the beam response during flexural tests of the section under minor-axis bending with the lips in compression, along with the corresponding force-deformation responses. The peak loads for all three specimens were closely similar: 5.2 kips in the first test, 5.3 kips in the second test, and 5.3 kips in the third test. The observed buckling patterns closely resembled the distortional buckling (D2) predicted by buckling analysis, with failure initiating through plastic deformation mechanisms in the return lips.

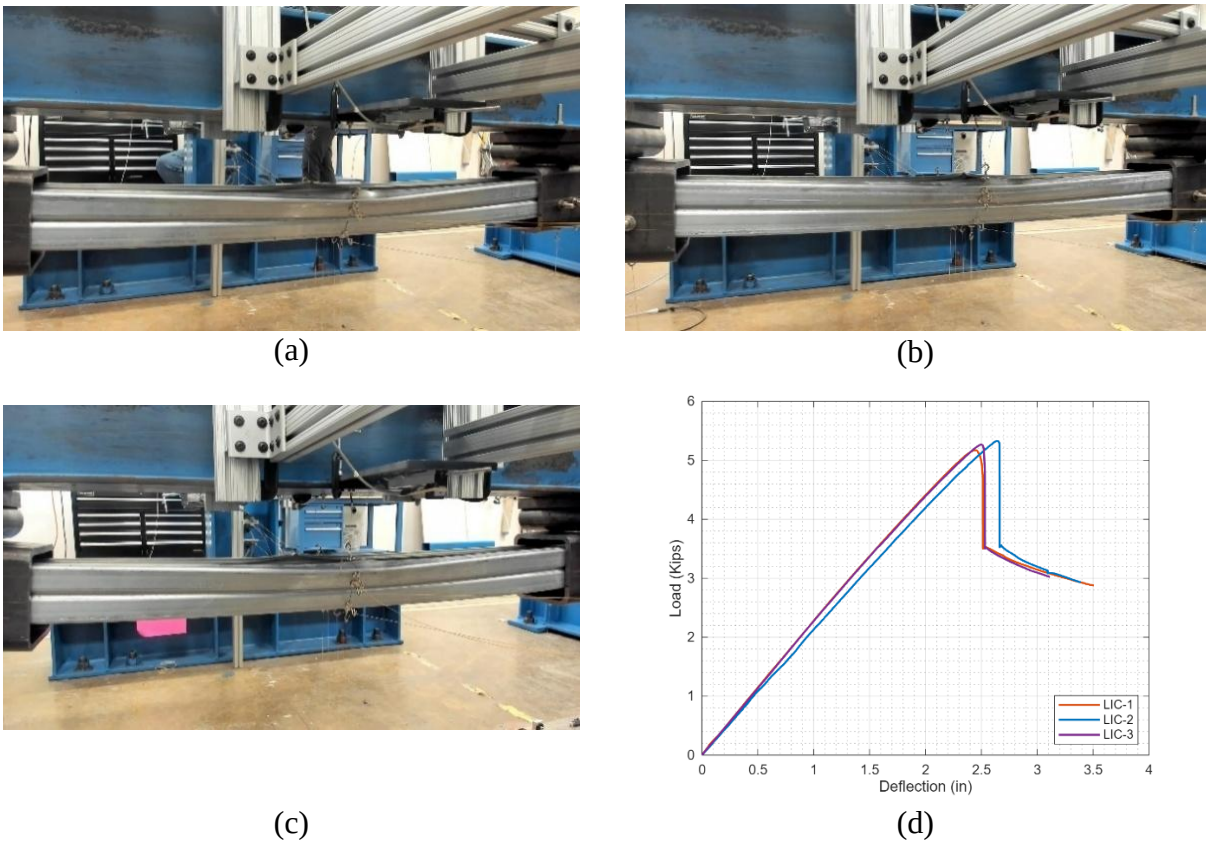

Figure 15. Post failure images from the minor-axis tests with section lips in compression: (a) LIC-1, (b) LIC-2, (c) LIC-3, and (d) Actuator load-deflection plots

5.2 Test results of minor axis bending with lips in Tension (LIT)

Figure 15 presents images of the beam's post-failure response from flexural tests of the section under minor-axis bending with the lips in tension, alongside the corresponding force-deformation curves. As observed, all three specimens exhibited nearly identical peak loads: 6.44 kips in the first test, 6.60 kips in the second test, and 6.63 kips in the third test. The observed buckling shape closely matched the distortional buckling mode predicted in the buckling analysis. During testing, three sequential failures of the web stiffeners along the moment span were observed, each reflected as a dip in the force-deformation curve prior to reaching the maximum load. Ultimately, the specimen failed by forming a roof-like collapse mechanism.

(a)

(b)

(c)

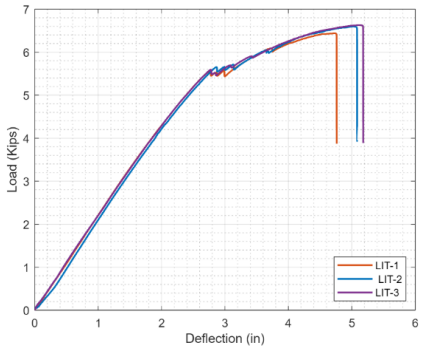

(d)

Figure 16. Post failure images from the minor-axis tests with section lips tension: (a) LIT-1, (b) LIT-2, (c) LIT-3, and (d) Actuator load-deflection plots

5.3 Test results of major axis bending with no decks on the shear spans

Pictures of the beam response during flexural tests of the section in major-axis bending without steel deck panels in the shear spans are provided in Figure 18, along with the force-deformation response. All three bending tests exhibited similar failure mechanisms, characterized by the combination of lateral-torsional buckling (LTB) and distortional buckling (D2) involving the top flanges at large angles of twist. In all three tests, both beams failed simultaneously at the loading points, displaying consistent failure patterns. The peak loads achieved during the tests were 14.2 kips in the first test, 14.3 kips in the second test, and 14.3 kips in the third test. The twist is continuous along the specimens including through the load point – so the moment span is not isolated, and the full span is participating in the response.

(a)

(b)

Figure 17. Post failure images from the major-axis tests without steel deck panels: (a) Major-1, (b) Major-2, (c) Major-3, and (d) Actuator load-deflection plots (continued)

(c)

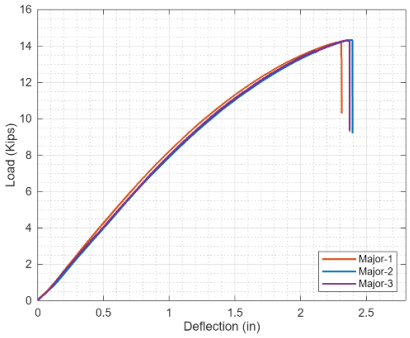

(d)

Figure 18. Post failure images from the major-axis tests without steel deck panels: (a) Major-1, (b) Major-2, (c) Major-3, and (d) Actuator load-deflection plots

5.4 Test results of major axis bending with decks on the shear spans

Figure 19 shows the beam response during flexural tests of the section in major-axis bending, where steel deck panels were added in the shear spans to stabilize the specimen, and the associated force-deformation response. The addition of the steel deck panels increased the torsional stiffness and isolated the primary response to the moment span resulting in higher peak loads of 16.3 kips for the first test, 16.2 kips for the second test, and 16.3 kips for the third test. Buckling waves associated with both distortional buckling modes (D1 and D2) were observed; however, the failure mechanism was primarily linked to the distortional buckling mode (D2) involving the twisting of the top flange, as identified in the buckling analysis (Figure 12).

(a)

(b)

(c)

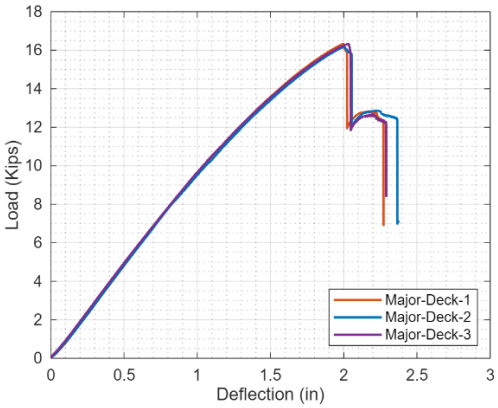

(d)

Figure 19. Post failure images from the major-axis tests with steel deck panels fastened onto the shear spans: (a) Major-Deck-1, (b) Major-Deck-2, (c) Major-Deck-3, and (d) Actuator load-deflection plots

6. Moment-Rotation Calculations

Moment vs. chord rotation relationships were derived using deflection measurements recorded by position transducers at the loading points, along with load data from the in-line load cell connected to the actuator, as shown in Figure 19. Figures 20 through 24 present the moment-rotation plots for all major- and minor-axis bending tests. A summary of the test-to-predicted moment capacity ratios is provided in Table 3.

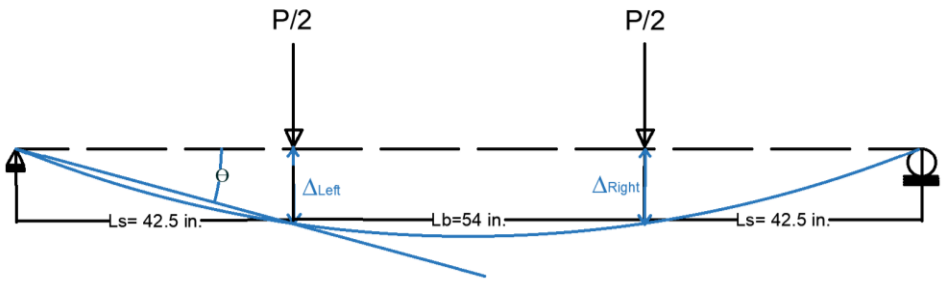

Figure 20. Schematic of beam chord rotation

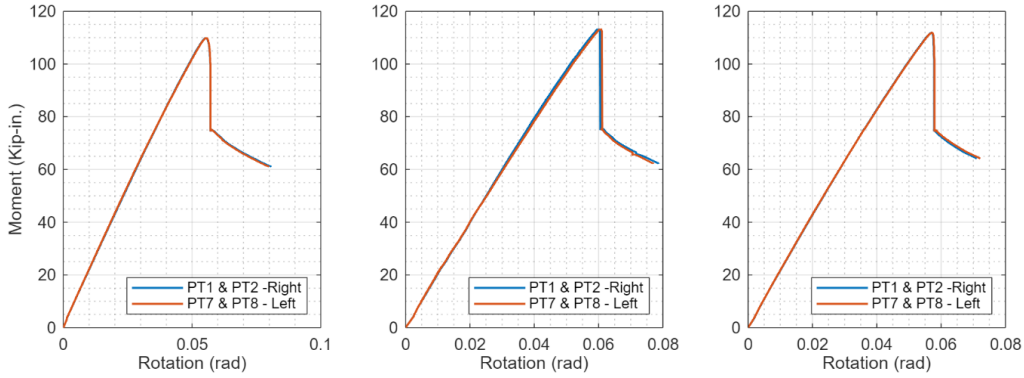

Figure 21. Moment-Rotation plots of the minor axis bending tests with Lips in compression: (a) LIC-1, (b) LIC-2, (c) LIC-3

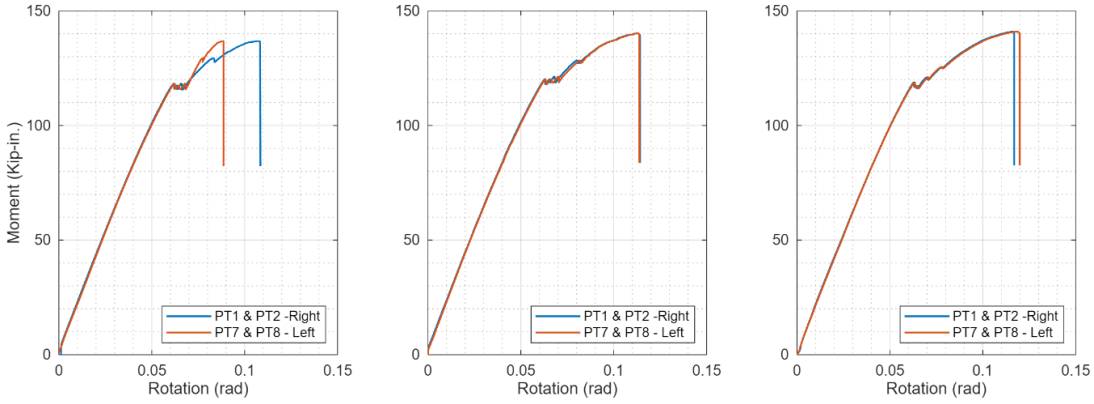

Figure 22. Moment-Rotation plots of the minor axis bending tests with Lips in tension: (a) LIT-1, (b) LIT-2, (c) LIT-3

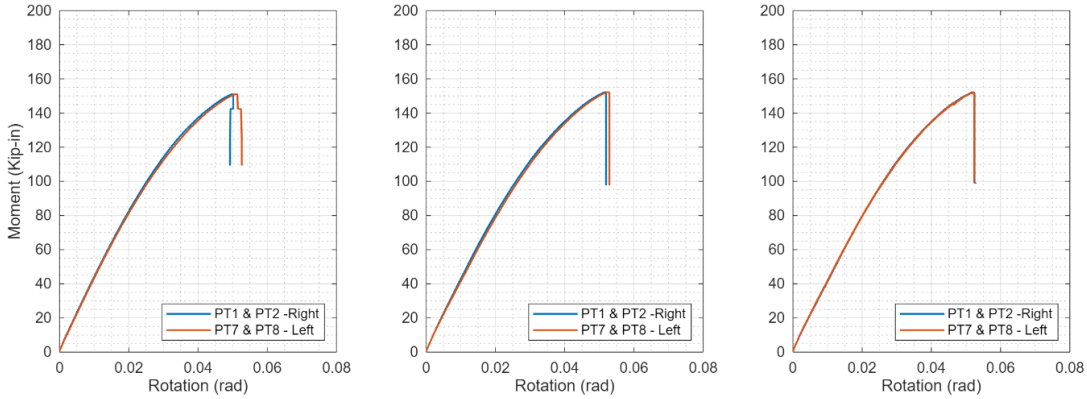

(a) (b) (c)

Figure 23. Moment-Rotation plots of the major axis bending tests with no decks: (a) Major-1, (b) Major-2, (c) Major-3

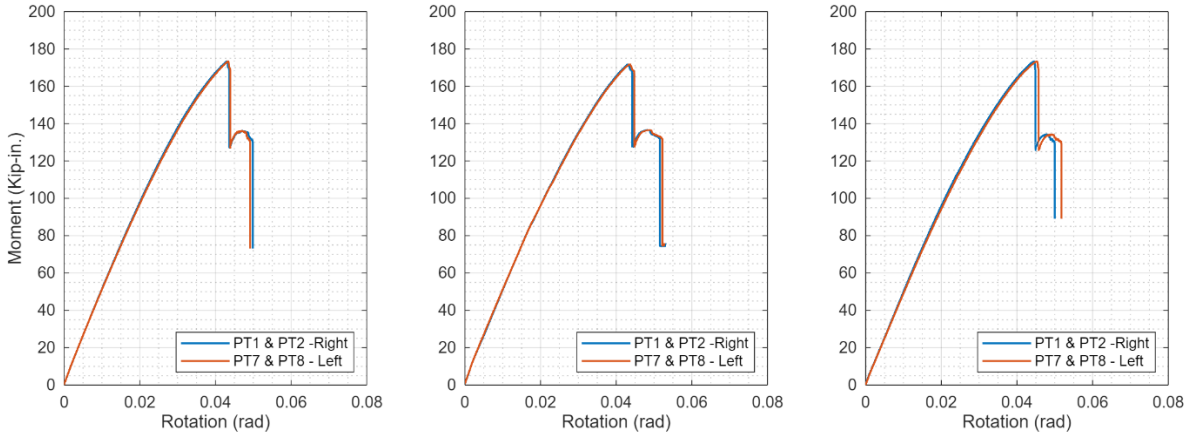

(a) (b) (c)

Figure 24. Moment-Rotation plots of the major axis bending tests with steel decks: (a) Major-Deck-1, (b) Major-Deck-2, (c) Major-Deck-3

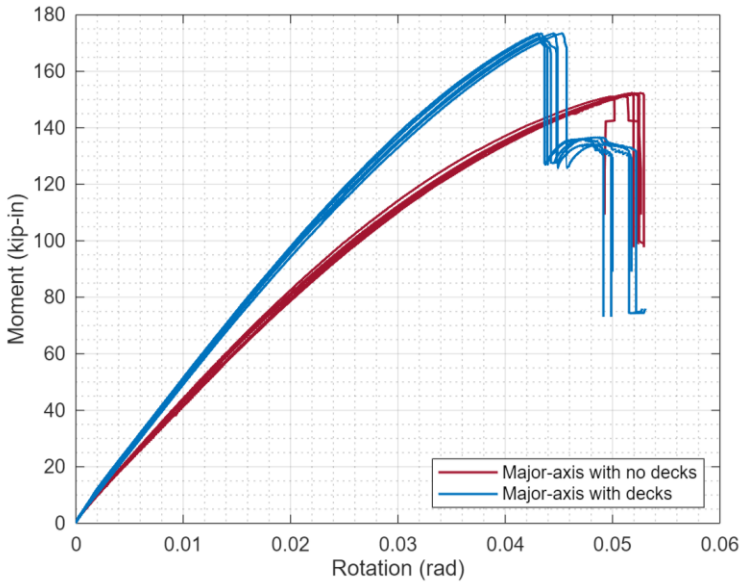

Figure 25. Left and right chord rotations from all tests in both major-axis test configurations: with and without decks fastened in the shear spans

Table 3. Summary of test to predicted capacity ratios

Test	$M_{max,\ test}$ (kip in.)	Controlling Mode	DSM S100-16 M_{test}/M_n	Glauz &Schafer (2022) M_{test}/M_n
Minor-LIC-1	109.93		1.29	1.18
Minor-LIC-2	113.23	D2	1.33	1.21
Minor-LIC-3	111.90		1.32	1.20
Mean	111.69		1.32	1.20
STD	1.660		0.02	0.02
CoV (%)	1.487		1.49	1.49
Minor-LIT-1	136.84		1.33	1.06
Minor-LIT-2	140.30	D	1.36	1.09
Minor-LIT-3	140.00		1.36	1.08
Mean	139.05		1.35	1.08
STD	1.917		0.02	0.01
CoV (%)	1.379		1.38	1.38
Major-1	151.05		0.86	0.87
Major-2	152.30	D2	0.86	0.87
Major-3	152.25		0.86	0.87
Mean	151.87		0.86	0.87
STD	0.708		0.004	0.004
CoV (%)	0.466		0.466	0.466
Major-Deck-1	173.30		0.98	0.99
Major-Deck-2	171.80	D2	0.97	0.98
Major-Deck-3	173.40		0.98	0.99
Mean	172.83		0.98	0.99
STD	0.896		0.006	0.006
CoV (%)	0.519		0.591	0.585

7. Discussion

7.1 Minor-axis bending tests lips in compression

Minor-axis bending tests with the lips in compression showed consistent behavior with failures initiated through plastic deformation mechanisms in the return lips. Observed buckling waves closely matched the predicted distortional buckling waves by buckling analysis. The bending capacities for the three tests were: 109.9 kip-in, 113.3 kip-in, and 111.9 kip-in. However, these capacities were lower than the nominal strengths predicted using the DSM as implemented in AISI S100, with a mean test-to-predicted ratio of 1.32. Comparatively, the proposed Glauz & Schafer (2022) DSM predictions for unsymmetric bending resulted in a mean test-to-predicted ratio of 1.20. It can be concluded that the current DSM method to predict the minor-axis flexural capacity of the section's lips in compression is unconservative and the Glauz & Schafer modifications are an improvement, but further refinement may be possible.

7.2 Minor-axis bending tests lips in tension

For minor-axis tests with lips in tension, a characteristic roof-like failure mechanism was observed in the web, preceded by stiffener failures at different locations along the moment span before reaching the peak load. The bending capacities recorded from the three tests were 136.84 kip-in, 140.3 kip-in, and 140.0 kip-in. Predictions by the DSM in AISI S100 were conservative, with a mean test-to-predicted ratio of 1.35. The Glauz & Schafer (2022) DSM predictions were more accurate, but still marginally conservative, with a mean test-to-predicted ratio of 1.08

7.3 Major-axis bending tests without steel deck panels in shear span

Major-axis bending tests conducted without steel deck panels in the shear span exhibited consistent failure mechanisms characterized by a combination of distortional buckling and lateral-torsional buckling, accompanied by significant twist. The peak flexural capacities recorded for the three tests were 151.1 kip-in, 152.3 kip-in, and 152.25 kip-in. The boundary conditions in the moment span do not meet the assumptions of the AISI Specification as they did not provide effective lateral support and predictions using the AISI S100 Direct Strength Method (DSM) were unconservative, with a test-to-predicted ratio of 0.86, or 0.87 when using the Glauz & Schafer (2022) DSM.

7.4 Major-axis bending tests with steel deck panels in shear span

Major-axis bending tests, with steel deck panels fastened at the top and bottom of the specimens in the shear spans, effectively restrained twist in the shear span. Under these conditions, failure was consistently associated with the distortional buckling mode. The peak flexural capacities recorded for the three tests were 173.3 kip-in, 171.8 kip-in, and 173.4 kip-in. The test results showed good agreement with predictions, with mean test-to-predicted ratios of 0.99 (by AISI S100 DSM) and 1.01 (Glauz & Schafer, 2022).

8. Conclusions

This study investigated the flexural strength of highly optimized, locally stiffened, lipped channel sections made from high-strength, low-alloy steel. A series of four-point bending tests were conducted to evaluate both major-axis and minor-axis flexural behavior. Given the high susceptibility of these sections to local and distortional buckling, special care was taken during testing to develop these failure modes while minimizing lateral-torsional buckling. Flexural

strength predictions were performed using the Direct Strength Method (DSM) in AISI S100-16 and the modified DSM approach by Glauz & Schafer (2022). The results indicate that the standard DSM method in AISI S100-16 and modified DSM approach by Glauz & Schafer (2022) provides reliable strength predictions when bending occurs about a symmetric axis for members braced against lateral torsional buckling mode. However, for bending about an unsymmetric axis, the modified DSM method by Glauz & Schafer (2022) offers more accurate capacity estimates especially for the minor axis bending with section lips in tension.

Acknowledgments
The authors would like to acknowledge Nucor Corp. for providing the specimens tested in this study, Damir Akchurin for sharing his experience in previous testing and analysis of these specimens in compression, and Dr. Sandor Àdàny for discussions related to global buckling.

References

Ádany, S. (2006). Buckling analysis of cold-formed steel members using CUFSM: conventional and constrained finite strip methods.

Akchurin, D., Torabian, D, Ding, C., Schafer, B. 2023. Compressive Capacity of Cold-Formed Steel High Strength Low-Alloy Lipped Channels with Intermediate Stiffeners. JHU Cold-Formed Steel Research Consortium (CFSRC). https://jscholarship.library.jhu.edu/handle/1774.2/40427

Akchurin, D., Torabian, S., & Schafer, B. W. (2025). High-strength cold-formed steel stiffened channel section: Axial compressive strength and initial geometric imperfections. Thin-Walled Structures, 206, 112604.

Glauz, R. S., & Schafer, B. W. (2022). Modifications to the direct strength method of cold-formed steel design for members unsymmetric about the axis of bending. Thin-Walled Structures, 173, 109025.

Li, Z., & Schafer, B. W. (2010). Buckling analysis of cold-formed steel members with general boundary conditions using CUFSM conventional and constrained finite strip methods.

North American, Specification for the Design of Cold-Formed Steel Structural Members, S100-16, American Iron and Steel Institute, Washington, DC, 2016.

Schafer, B. W., & Adany, S. (2005). Understanding and classifying local, distortional and global buckling in open thin-walled members. *Tech. Session and Mtg., Structural Stability Research Council. Montreal, Canada*.

Yu, C. (2005). Distortional buckling of cold-formed steel members in bending. The Johns Hopkins University.

Yu, C., & Schafer, B. W. (2007). Simulation of cold-formed steel beams in local and distortional buckling with applications to the direct strength method. Journal of Constructional Steel Research, 63(5), 581-590.